Laser metal deposition as repair technology for Inconel 718

Lorena Cano-Salinas, Mehdi Salem, Kamel Moussaoui, Sabine Le Roux, Anis Hor, Redouane Zitoune

The International Journal of Advanced Manufacturing Technology
https://doi.org/10.1007/s00170-024-14982-x

ORIGINAL ARTICLE

Laser metal deposition as repair technology for Inconel 718

Lorena Cano-Salinas[1] · Mehdi Salem[1] · Kamel Moussaoui[1] · Sabine Le Roux[1] · Anis Hor[1] · Redouane Zitoune[1,2]

Received: 23 July 2024 / Accepted: 25 December 2024

Abstract
From an economic and sustainability point of view, repair is considered a promising alternative for high value-added aeronautical materials. In this study, laser metal deposition (LMD) was used for simulating the repair of damaged Inconel 718 (IN718) parts. Grooves were machined in IN718 substrates using abrasive water jet (AWJ) and filled with powdered IN718 alloy. Based on these results, a set of optimal LMD process parameters were selected for depositing material layers on milled substrates with various of roughness and texture levels induced by AWJ machining to evaluate the effect of surface preparation on repair quality. The substrate-deposit repair interfaces were characterized using microscopic analysis and multi-scale hardness tests. The results showed the influence of scan speed on the height of the weld bead, while increasing laser power and scan speed were both found to increase weld bead height. Dilution increased with a decrease in scan speed. Additionally, repair quality was found to be independent of the different surface conditions. Overall, the repairs exhibited excellent weldability, and were free of cracks and lack-of-fusion defects. Furthermore, microhardness measurements yielded higher values of hardness in the deposit area than in the substrate for all repairs.

Keywords Repair · Laser metal deposition · AWJ milling · Inconel 718 · Sustainability

1 Introduction

Laser metal deposition (LMD) is a directed energy deposition (DED) technique which uses a laser beam as thermal source to melt powdered feedstock fed through a nozzle onto a substrate. As the nozzle and laser beam move along a raster pattern, a weld bead is created on the surface of the substrate. A part may then be built by depositing successive layers.

The circular economy strategy can significantly contribute to increasing the environmental sustainability of products. The processes of repair, refurbishment, and remanufacturing aim at restoring the intrinsic value of a part that has degraded through normal and/or artificial wear and tear throughout its lifecycle. Re-using production material from an existing part and repairing damaged components are clearly desirable from both economic and ecological points of view, since they contribute to sustainable development. Repairing damaged parts can be achieved using additive manufacturing (AM) processes [1]. The LMD process can be used to build components with complex geometries or repair worn-out parts such as turbine blades and blisks [2–4]. In recent years, LMD has gained interest as a repair application because it allows considerable cost savings in terms of manufacturing time, since only the damaged volume is restored instead of the full component [5]. There are also specific challenges linked to repair like deep learning for automatic damage detection [6] and adaptive hybrid process chains which reduce process variations in LMD [7]. A reverse engineering approach for reconstructing surface topology from spatial measurements may also be used for enhancing the remanufacturing of worn-out parts [8, 9].

Inconel 718 (IN718) is a Ni-based superalloy commonly used for aircraft parts exposed to harsh environments, due to its high strength and resistance to corrosion at operating temperatures up to 700°C [2, 5, 10].

Due to the various process parameters involved in the LMD process, of which scanning speed and powder feed rate are key, it is currently challenging to predict the end

✉ Redouane Zitoune
Redouane.zitoune@iut-tlse3.fr

[1] Institut Clément Ader (ICA), Université de Toulouse, CNRS, INSA, ISAE-SUPAERO, Mines-Albi, UPS, 3 Rue Caroline Aigle, 31400 Toulouse, France

[2] CNRS-International-NTU-THALES-Research-Alliance (CINTRA, UMI 3288), Nanyang Technological University, Nanyang, Singapore

Published online: 04 January 2025

properties of the deposited filler material [11]. Furthermore, a current concern in LMD is the transfer of optimum parameters between different manufacturing systems not being sufficiently characterized [11]. The complexity of manufacturing processes can lead to increased scrap and rework, prompting the development of predictive models like machine learning approach to enhance the understanding and prediction of part properties prior to production [12].

Extensive research on the microstructure and mechanical properties of laser metal deposited IN718 has been achieved [3, 10, 13–18]; however, limited literature is available on substrate-deposit interface characterization [2, 5, 19, 20], particularly with regard to the repair process. The mechanical properties of an LMD-repaired part, to which the microstructure is related, are highly influenced by the process parameters used and are commonly used to validate the repair. We also find studies on the effect of process parameters on bead geometry [21, 22] where it is shown that laser power and scanning speed significantly affect track width, height, and penetration depth. Track width is notably influenced by the interplay of both the parameters. Mazzucato et al. [23] studied the mechanical characterization of LMD-ed Inconel 718. They showed that the strain hardening capacity of as-built samples improves with increased laser power during the LMD process, with specimens deposited using laser power of 400W achieving an average yield strength of 703 MPa.

The microstructure of LMD-ed material depends on its complex thermal history—a mix of thermal gradients and cooling rates that take place during the deposition process [11]. Generally, columnar dendrites form at high temperature gradients and low solidification rates, whereas equiaxed dendrites form at low thermal gradients and high cooling rates. A mixture of columnar and equiaxed dendrites may also occur. Grain growth occurs mainly along the direction of maximum heat flow [24]. Studies on the microstructure of IN718 at the substrate-deposit interface [2, 5, 14, 20, 25, 26] showed a columnar grain structure growing epitaxially from the substrate. In [2, 14] the researchers reported slightly larger equiaxed grains at the substrate-deposit interface, due to the metallurgical bond as laser radiation extends into the substrate, creating a heat affected zone (HAZ).

Further research into the microstructure of IN718 has shown Laves phases, carbides and δ phase as the main precipitates formed by micro-segregation of niobium (Nb), molybdenum (Mo) and titanium (Ti) in the inter-dendritic regions and along the grain boundaries of the deposited material [2, 3, 10, 13, 25, 26]. Laves phase can occur in a continuous or discontinuous manner: fast cooling rates, for instance, promote a continuous distribution of Laves [2].

Porosity in the microstructure of LMD-processed parts is a major drawback. Literature reports that higher laser power favours the occurrence of porosity through turbulence in the melt pool, leading to gas entrapment during the process [3]. However, low values of laser power may also prove insufficient, creating partial melting zones and thereby porous structures [27]. Porosity may be further attributed to defects originally present in the powdered feedstock [3, 28], which then form voids at the substrate-deposit interface. Liu et al. [29] evaluated the repair over improperly machined cavities, including indentations, grooves and through-holes, in gas turbine engine components made of Inconel 718 and reported excellent weldability with no lack-of-fusion defects, except for some minor porosity in repaired through-holes. Onuike and Bandyopadhyay [5] used LMD to repair rectangular- and trapezoidal-shaped IN718 cavities. They reported void inclusion defects attributed to sharp-angle boundary restrictions that shielded off some metal powders when refilling the rectangular cavity. Trapezoidal slots showed good material fusion without any void inclusion. Johnson et al. [15] reported lack-of-fusion defects between the substrate and early deposited layers, attributed to the non-preheated substrate, thereby creating melt pool instability, mostly likely a result of higher cooling rates along the substrate surface.

Microhardness test results for laser-deposited IN718 onto IN718 substrate are scarcely found in existing literature to date. In [17, 20, 26] higher Vickers hardness values were reported in the substrate than in non-heat treated deposit areas. When using laser power of *1100 W*, Tabernero et al. [20] obtained ~ *400 HV* in the substrate and ~ *200 HV* in the deposit, whilst Lambarri et al. [26] found a microhardness value in the substrate of ~ *300 HV* against ~ *220 HV* in the deposit, attributing the higher hardness in the substrate to twinning. Kumar and Nair [19] studied the effect of LMD parameters on the inter-layer bonding in deposited IN718 for refurbished IN718 components. They reported that laser power of *2350 W*, scan speed of *700 mm/min* and powder feed rate of *10 g/min* were the optimum parameters to obtain the highest hardness of *300 HV* within their process parameter window. Onuike and Bandyopadhyay [5] presented a hardness profile where the hardness did not vary significantly across the interface, with an average value of *2.6 GPa* between the substrate and the deposit.

Even though some studies focus on the properties of the substrate-deposit interface for deposited IN718 material, a gap persists with regard to substrate machining and the LMD process as coupled stages in the repair process chain. Some exceptions are the studies carried out by Onuike et al. [5] and Liu et al. [29].

The aim of the present investigation is to first design a full factorial experimental design for the IN718 alloy, i.e., using three levels of laser powder and scanning speed each, to find a set of optimal process parameters for the LMD repair process, with respect to the geometrical characteristics of a single weld bead. Then, multi-layered geometries will be LMD-deposited using IN718 powder onto seven

Table 1 Chemical composition (%wt) of the IN718 powder and substrate

	Ni (%)	Cr (%)	Fe (%)	Nb (%)	Mo (%)	Ti (%)	Al (%)	Co (%)	C (%)	Mn (%)	Si (%)
Substrate	53.47	18.28	18.2	5.06	2.98	0.96	0.51	0.17	0.03	0.09	0.08
Powder	52.8	19.2	17.8	5.29	3.1	1.0	0.6	0.0	0.05	0.02	0.10

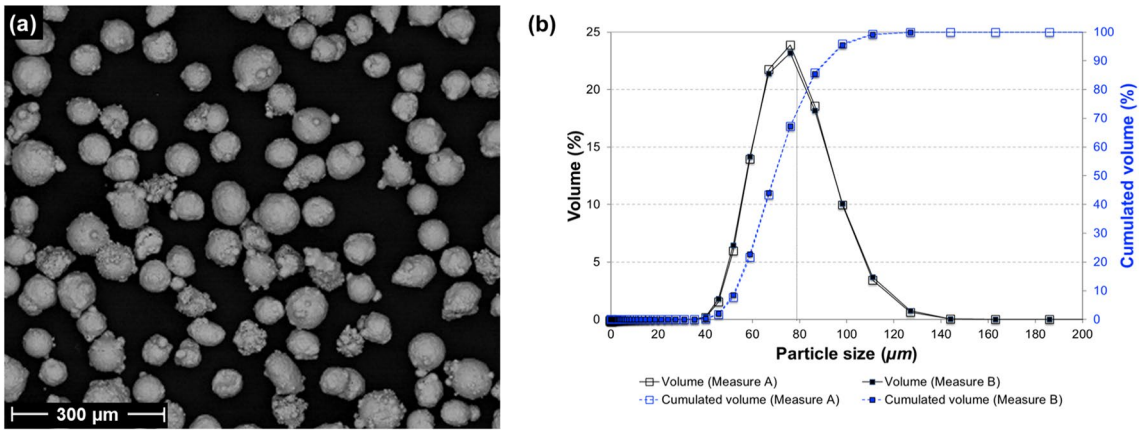

Fig. 1 SEM micrographs (BSE mode) of the IN718 powder (**a**) morphology in × 130 magnification; **b** graph of powder size distribution measured using the laser technique

differently-milled (in terms of roughness and texture induced by abrasive water jet (AWJ) machining) IN718 substrates, to examine the substrate-deposit interface for variations in microstructure, porosity and micro-hardness along both parallel and perpendicular cross-sections (with respect to the direction of deposition). This will allow the quality of the repaired interface to be validated in view of potential aeronautical applications.

2 Experimental procedure

2.1 Materials and methods

Inconel alloy 718 (IN718) was used in this investigation both in the wrought substrate andin the gas-atomized powder feedstock. Commercially available Inconel 718 powder supplied by Höganäs Germany GmbH Company was used, with a composition matching that of the substrate. The chemical compositions of the powder and substrate are given in Table 1. The particle size distribution was analysed using a laser technique, where optical properties are derived from the interaction between a set of powder particles and an incident laser beam to obtain the size distribution. The median size of the IN718 powder particles was found to be ~ *80 µm*, with 90% of particles falling within the size range of *60–100 µm* (Fig. 1b). Powder particles had a predominantly spherical shape, with satellite particles attached (Fig. 1a).

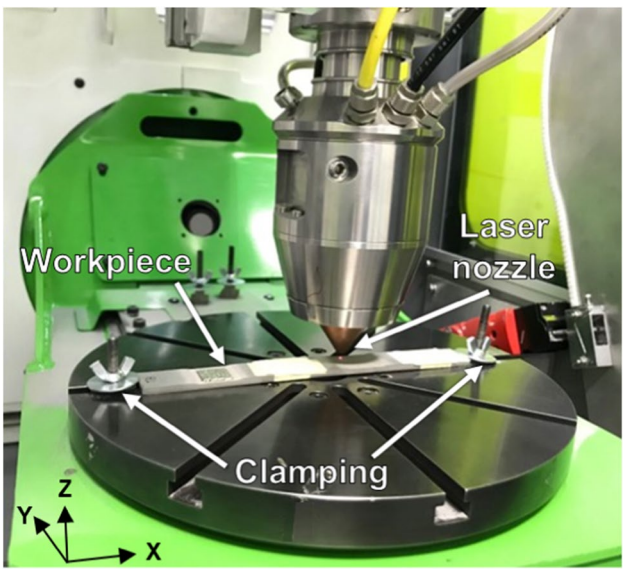

Fig. 2 Overall view of the experimental setup for Laser Metal Deposition process

A BeAM Machine Mobile 1.0 with a 500 W Nd:YAG CW laser and a five-axis numerical control was used to perform the deposits. Argon was used as both carrier and shielding gas, to prevent oxidation and contamination. The laser beam was focused to a spot size of *0.8 mm*. The overview of the experimental setup is shown in Fig. 2.

To select an optimal set of parameters, the geometrical characteristics and dilution (depth of melt pool) of single weld beads were first examined. Several weld beads were deposited on wrought IN718 substrate by varying laser power and scanning speed. The weld beads were 20 mm-long and spaced 3mm apart on the substrate. A relatively large window of operation was outlined to select the optimal laser power and scanning speed, in line with the manufacturer's recommendations for IN718. The laser power input varied between *250* and *300 W*, the scanning speed varied from *400* to *1000 mm/min*, and the powder feed rate was fixed at a constant value of *5.5 g/min*, resulting in twelve different parameter sets. The parameters used to build the single weld beads are summarized in Table 2. For reliability, three weld beads were built with the same set of parameters, resulting in thirty-six weld beads in total. The dimensions of width and height, the dilution and input linear energy of the weld beads were then analyzed to identify a suitable set of parameters for performing further repair experiments.

Substrates of wrought IN718 were machined in a non-conventional manner prior to the LMD process as part of the repair process chain. The substrates were milled using AWJ to create seven different "blind" pockets of 20×20 *mm* (Fig. 3a) each machined using different values of water pressure (P), traverse speed (f) and step-over distance (STD), which resulted in different pocket depths, and different surface texture and roughness of the pocket bottom as listed in Table 3.

Table 2 Input parameters of as-deposited Inconel 718 by laser additive manufacturing

Laser power (*W*)	Scanning velocity (*mm/min*)	Powder feed rate (*g/min*)	Spot diameter (*mm*)
250, 275, 300	400, 600, 800, 1000	5.5	0.8

Table 3 Input parameters of AWJ process and output parameters of roughness and texture values [30]

P (MPa)	*f (m/min)*	*STD (mm)*	*Sa (μm)*	*Str*
200	1	1	13.23	0.89
200	1.5	1	12.96	0.93
250	0.5	1	18.30	0.64
250	0.5	1.5	18.24	0.16
250	1	0.5	13.50	0.42
300	0.5	1	20.71	0.34
300	0.5	1.5	18.39	0.15

These seven blind-pockets were then post-processed using plain water jet (PWJ) at $P = 200$ *MPa*, $f = 1$ *m/min*, $STD = 0.5$ *mm*, in order to remove the grit embedded by AWJ machining; however 4% of grit remained in all pockets. It should be mentioned that the surface texture and roughness, the depth of removed material and residual stresses induced by AWJ operation were almost unchanged after the PWJ cleaning process. Hence, the bottom of the blind-pockets was used as substrates for laser deposition, where five-layer square-shaped structures with dimensions 15×15mm were built in the middle of each pocket (Fig. 3a-b). In addition to the seven cuboids, two other cuboids were also deposited: one blind-pocket milled at $P = 200$ *MPa*, $f = 1$ *m/min*, $STD = 0.5$ *mm* and PWJ cleaned, to ensure repeatability, and another on wrought IN718 substrate for reference. Thus, these nine cuboids were all built using the parameter settings given in Table 4.

A bidirectional deposition pattern was used to perform the repair, and each layer was deposited parallel to the previous one. The laser scanning pattern was oriented along the y-axis (Fig. 3d), parallel to the direction of machining using AWJ and PWJ.

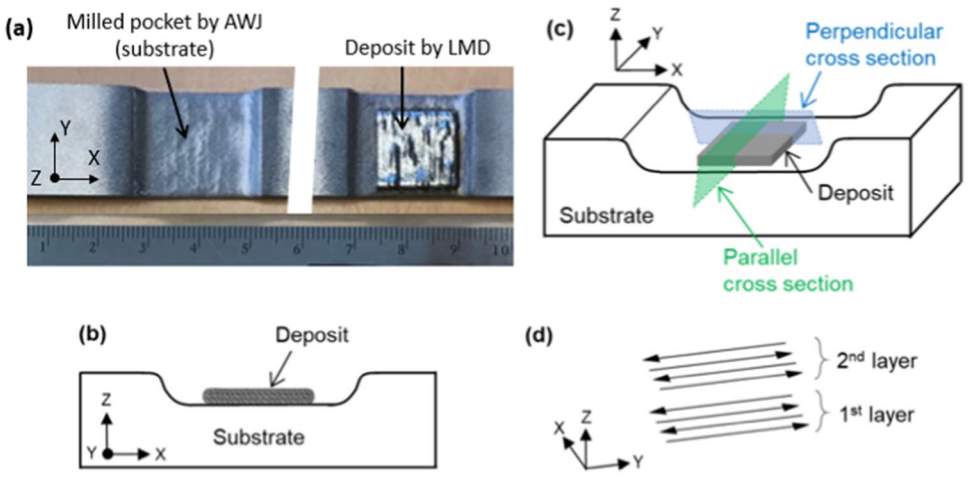

Fig. 3 **a** Overview of an example of a "blind" pocket and deposit; **b** schematic diagram showing a sample lateral view; **c** extracted cross-sectional sample schematic, and (**d**) the deposition strategy path

Table 4 Parameters used to build the cuboids

Laser power (*W*)	Scanning velocity (*mm/min*)	Powder feed rate (*g/min*)	Spot diameter (*mm*)	Increment of Z axis (*mm*)	Overlaps (%)
250	800	5.5	0.8	0.15	30%

2.2 Geometrical characteristics of single weld beads

The dimensional quality of single weld beads may be characterized using two main criteria: the aspect ratio (AR), which is the width-to-height ratio of the bead [32], and dilution (D), which is related to the melt pool depth, [33] as defined in Eqs. (1) and (2), where w is the width and h is the height of the weld bead, d is the depth of the melt pool and D is dilution.

$$A_R = \frac{w}{h} \tag{1}$$

$$D = \frac{d}{h + d} \tag{2}$$

An aspect ratio $A_R \geq 4$ is recommended due to less probability of porosity formation between the overlapped layers [32]. A dilution of less than 14% results in insufficient metallurgical bonding, and dilution values greater than 35% are not desirable due to downgraded deposition efficiency, and/or this may degrade the mechanical properties of the printed part due to the formation of a large HAZ [32]. In their studies on dilution, Dass et al. report the optimum value to lie between 10 and 30% [33]. The weld bead dimension measurements are summarized in Table 5. Linear energy (E) is calculated as the ratio of laser power to scanning speed. Excessive energy input could reduce the microstructural and mechanical performance of printed parts [28], thus,

Table 5 Geometrical dimensions and energy density of deposited single beads

Test	Laser Power *P* (*W*)	Scan velocity *V* (*mm/min*)	E (*J/mm*)	*AR*	*D*
(a)	250	400	37.5	2.61	0.26
(b)	275	400	41.3	2.62	0.24
(c)	300	400	45	2.86	0.23
(d)	250	600	25	4.03	0.38
(e)	275	600	27.5	4.01	0.39
(f)	300	600	30	4.48	0.41
(g)	250	800	18.8	4.84	0.46
(h)	275	800	20.6	4.86	0.46
(i)	300	800	22.5	5.28	0.46
(j)	250	1000	15	5.92	0.53
(k)	275	1000	16.5	6.08	0.54
(l)	300	1000	18	5.61	0.51

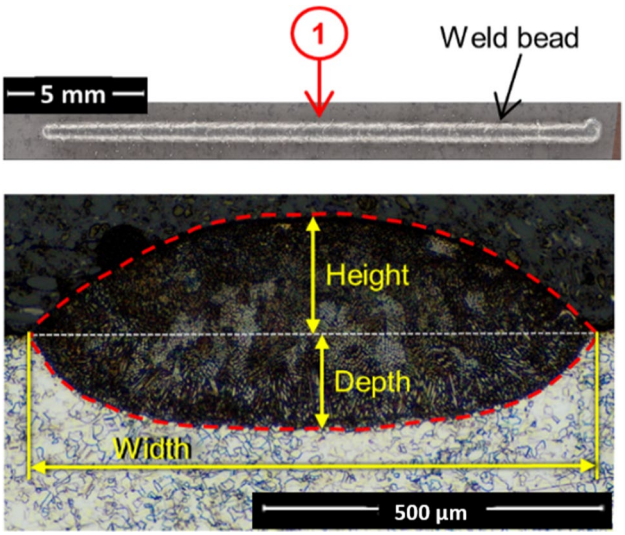

Fig. 4 Cross-section of a weld bead deposited using parameters P = 250W, v = 800 mm/min and Q = 5.5 g/min. The measurement positions (indicated by the red arrow) and geometrical dimensions were determined using an optical microscope

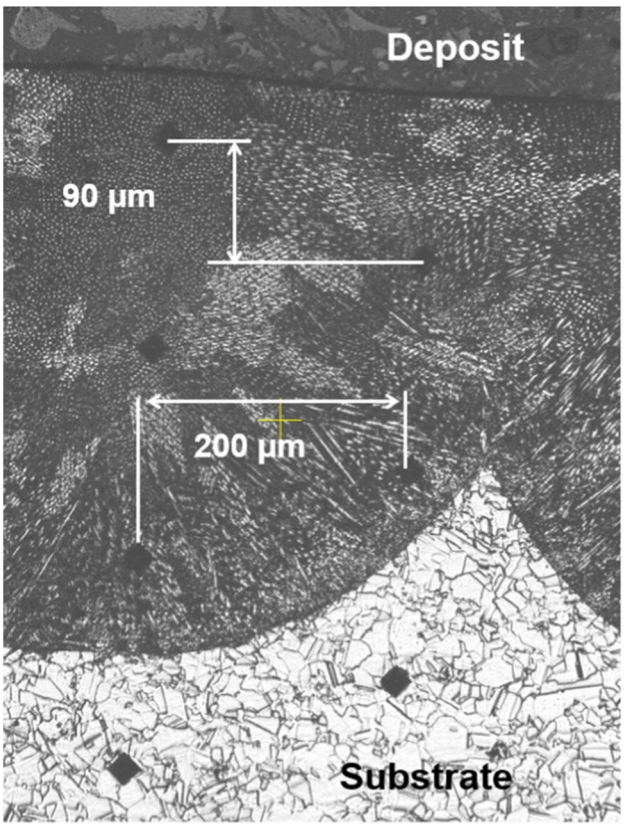

Fig. 5 Pattern used for indentation

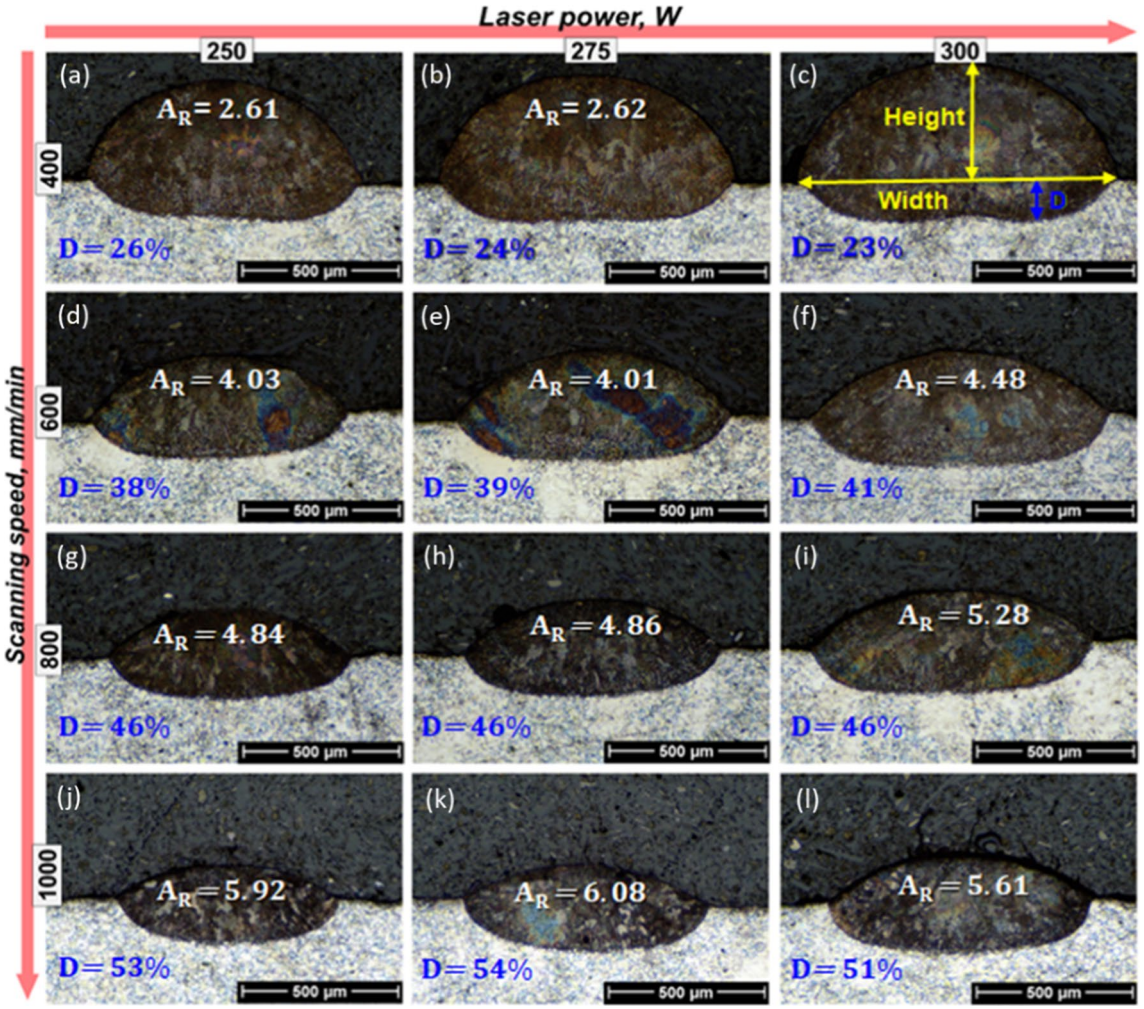

Fig. 6 Cross-sectional dimensions for weld beads printed using different sets of process parameters. With: (**a**), (**b**) and (**c**) conducted with a scanne speed of 400 mm/min and a power of 250 W, 275 W and 300 W respectively, (**d**), (**e**) and (**f**) conducted with a scanne speed of 600 mm/min and a power of 250 W, 275 W and 300 W respectively. (**g**), (**h**) and (**i**) conducted with a scanne speed of 800 mm/min and a power of 250 W, 275 W and 300 W respectively. (**j**), (**k**) and (**l**) conducted with a scanne speed of 1000 mm/min and a power of 250 W, 275 W and 300 W respectively

lower heat inputs are preferred for avoiding material distortion caused by overheating of the substrate or pre-deposited layers.

2.3 Surface characterization techniques and procedures

Geometrical dimensional characteristics of the single weld beads, including width, height, and depth of the melt pool, related to dilution, were characterised using destructive analysis methods. Each weld bead was cut transversally the resulting cross-section mounted in resin, ground and polished, then chemically etched using regal water in a 1:1 ratio during ~ 15 s in order to measure the dilution using an optical microscope. The cross-sections of all the weld beads were observed under an Olympus B41M-LED optical microscope to check for repeatability of the bead width and height, as well as the dilution values (Fig. 4). The mean width, height and dilution were obtained using measures from the three weld beads deposited using the same set of parameters.

Following the deposition process, each cuboid was cut using an abrasive cut-off wheel with water cooling, along two cross-sections, parallel (y) and perpendicular (x) to the build direction (Fig. 3c). These samples were mounted in thermosetting resin and ground with *SiC* papers of varying grits from *46* to *5 µm*, and then were polished to a mirror finish with *3 µm* diamond powder, followed by *1 µm*. For microstructural characterization, the samples were chemically etched with an acidic mixture of 5 ml H_2SO_4 + 3 ml

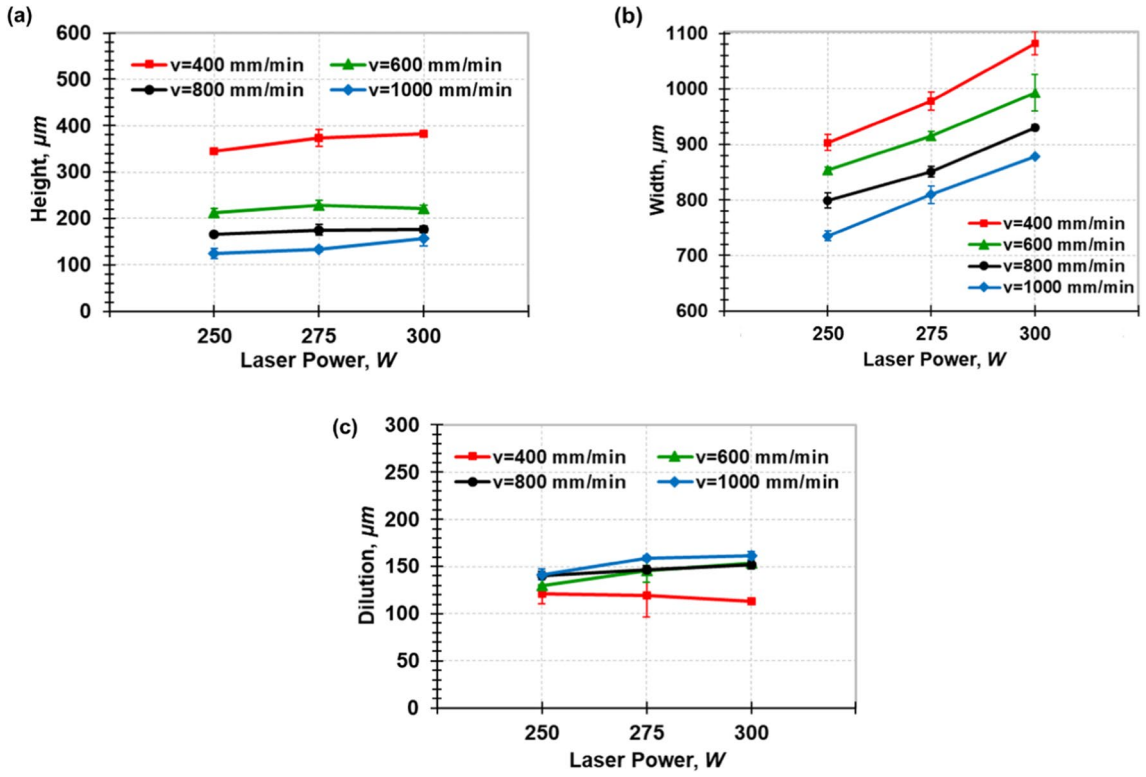

Fig. 7 The influence of laser power on (**a**) bead height, (**b**) bead width, and (**c**) melt pool depth, as observed at different scanning speeds

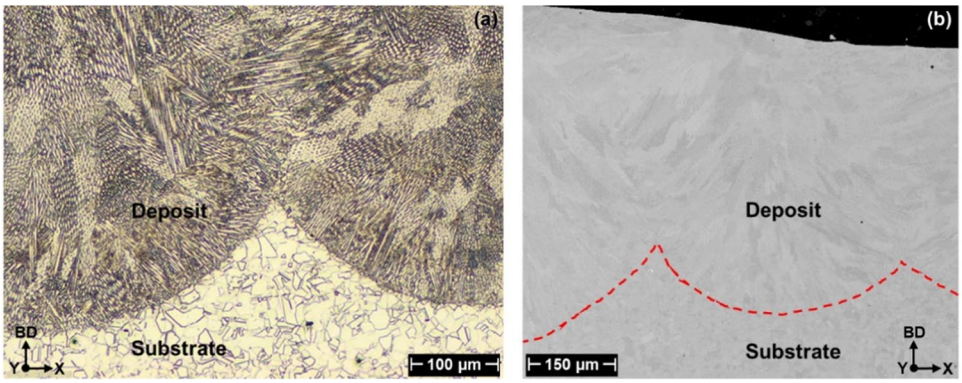

Fig. 8 Micrographs showing the substrate and deposit microstructures of substrates machined at (**a**) P = 300 MPa, f = 0.5 m/min and STD = 1 mm taken using an optical microscope, and at (**b**) P = 250 MPa, f = 1 m/min and STD = 0.5 mm taken using SEM, with the interface marked with a dotted red line

HNO_3 + 92 ml HCl by swabbing the polished surface with cotton soaked in etchant [31] between 15 s and 1 min. Microstructural characterization of the parallel and perpendicular cross-sections were performed using a HITACHI TM-3000 tabletop microscope and a Nova NanoSEM™ 450 Scanning Electron Microscope (SEM) equipped with BSE, SE and EDS detectors.

The cross-sections were then re-polished from the 1200 grit level to a mirror finish using *1 μm* diamond powder, followed by exposure to standard silica suspension (OP-S) during 30 min to obtain a final polished specimen for microhardness testing. Microhardness tests were performed by means of a Buehler Micromet 5104 apparatus. Hardness indentations were made with a load of *200 gf* applied during 10 s with a Vickers indenter in three filiations per cross-section in a zigzag pattern going from the deposited material towards the substrate, with vertical interval of 0.09 mm covering at least *200 μm* from the deposited material to the substrate (Fig. 5). Each filiation was separated by at least *200 μm* from the next. Cross-sections in both the x- and y-axis directions along the nine deposited cuboids were indented. Hardness measurement values were obtained for each cross-section as an average of the three indented filiations.

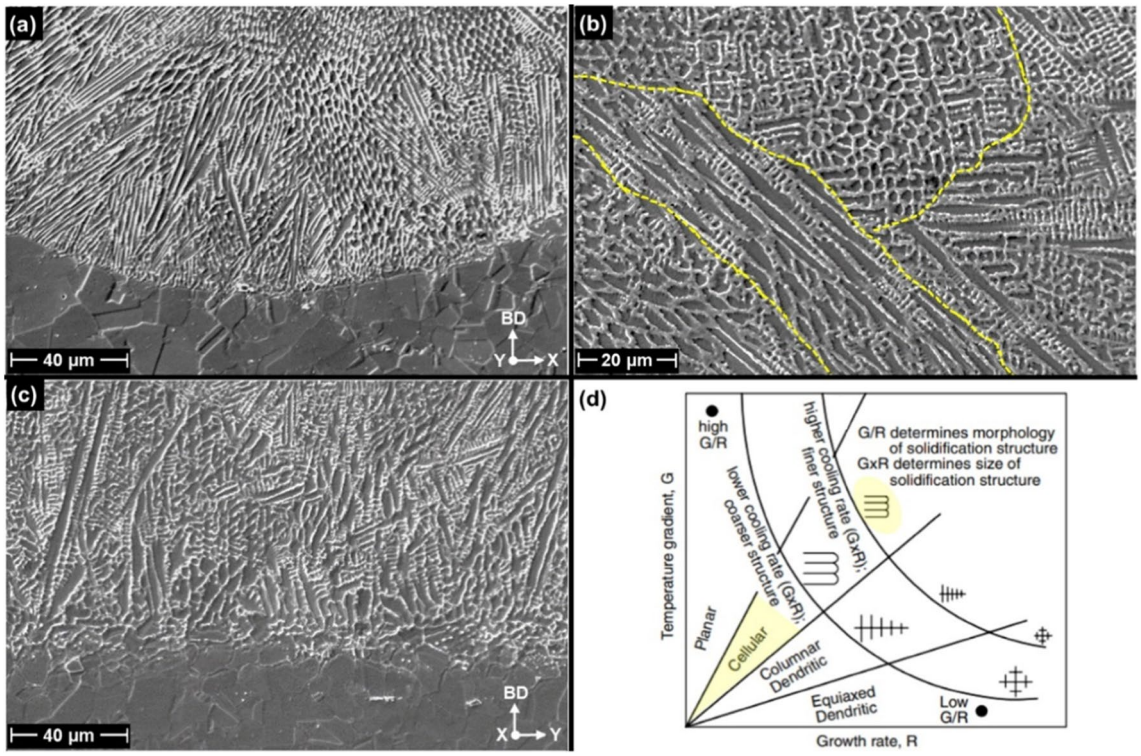

Fig. 9 SEM images (SE mode) showing microstructure of deposited material on different substrates machined at (**a**) P = 200 MPa, f = 1 m/min and STD = 1 mm, and (**b**) a magnification of a dendrite showing different cellular morphology according to the cutting plan; (**c**) P = 300 MPa, f = 0.5 m/min and STD = 1 mm; and (**d**) graph showing the effect of temperature gradient and solidification rate on grain morphology [34]

3 Results and discussion

3.1 Single weld beads

Figure 6 summarises the variation of the weld-bead cross-sections with increasing laser power and scanning speeds. It was observed that larger weld beads (height and width) may be obtained by simultaneously increasing laser power and decreasing scanning speed.

The influence of laser power and scanning speed on the height and width of the weld bead are summarized in Fig. 7a and b, as obtained using non-destructive analysis, and on the dilution in Fig. 7c, as obtained using destructive analysis. As shown in Fig. 7a, the height was found to be mainly influenced by scanning speed but almost unchanged by laser power. The bead width, on the other hand, varied with both laser power and scanning speed. Width was seen to increase with increasing laser power and decreasing scanning speed, as in Fig. 7b. Higher laser power results in more thermal energy being available, and this creates wider melt pools, and consequently, wider weld beads. Higher scanning speeds lead to the laser beam being incident on the substrate for a lower duration. Less substrate material gets melted and is available for fusion, leading to lower height and width of the weld beads. These trends were found to be consistent with those reported by Sreekanth et al. [21] who studied the influence of different process parameters on printed IN718 alloy. As depicted in Fig. 7c, the scanning speed has the greatest impact on dilution. Increasing scanning speeds result in deeper melt pools, while increasing laser power leads to only a slight increase in dilution at scanning speeds higher than 600mm/min, as seen in Fig. 7c.

To select the parameters to be used in the repair process, a trade-off between the criteria of width-to-height ratio, dilution and energy input was considered. Weld beads with AR ≥ 4 were identified in Fig. 6d-(l) and those with a suitable range of dilution, 14% < D < 35% in Fig. 6a-c. A criterion of 38% < D < 50% was considered acceptable due to high productivity rate being not essential, but the dilution being still low enough to prevent degradation of the mechanical properties. The beads in Fig. 6d-(i) were therefore considered to have acceptable levels of dilution. Lower energy input levels were preferred for keeping overheating and material distortion in the thin substrates at a minimum. These lower energy levels were found to occur because of lower laser power and higher scanning speed, corresponding to weld beads in Fig. 6g-(l). Overall, the

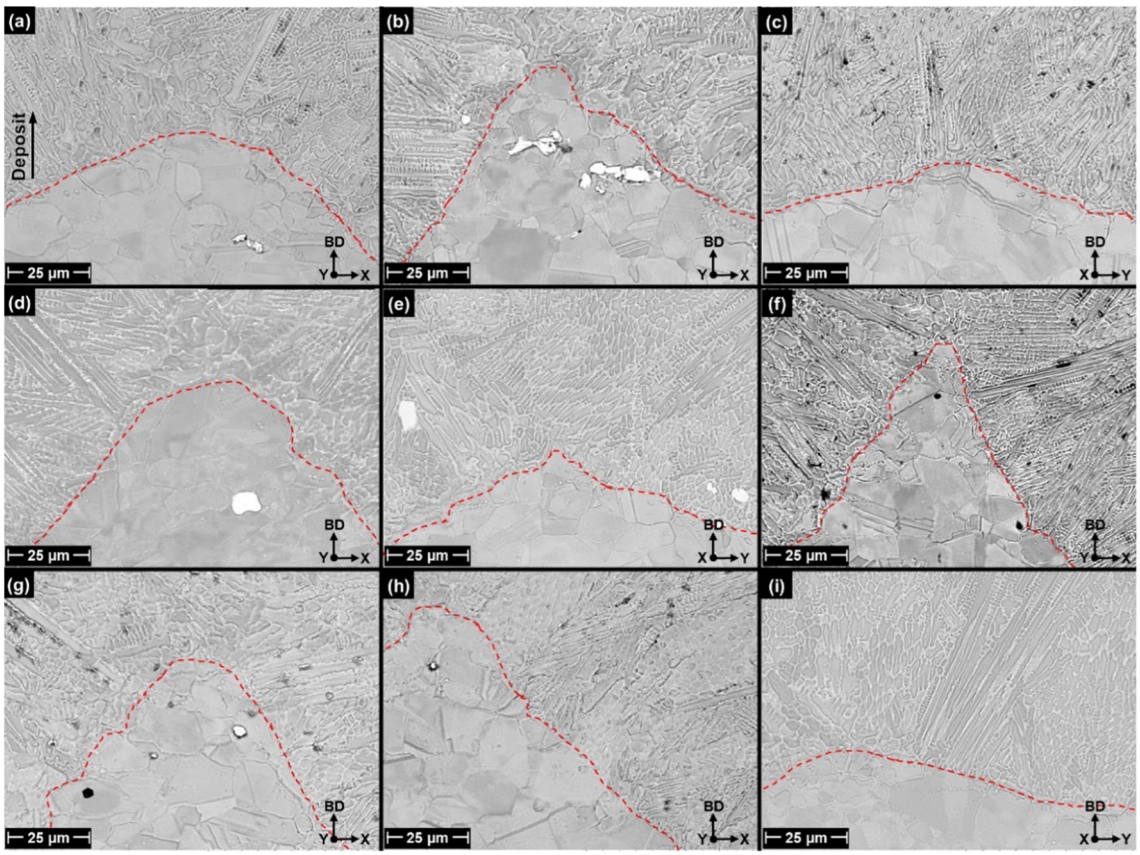

Fig. 10 SEM micrographs of the substrate-deposit interfaces for (**a**) bulk material substrate and, the substrates milled by AWJ at (**b**) P = 200 MPa, f = 1 m/min and STD = 1 mm; (**c**) P = 200 MPa, f = 1.5 m/min and STD = 1 mm; (**d**) P = 250 MPa, f = 0.5 m/min and STD = 1 mm; (**e**) P = 250 MPa, f = 0.5 m/min and STD = 1.5 mm; (**f**) P = 250 MPa, f = 1 m/min and STD = 0.5 mm; (**g**) P = 300 MPa, f = 0.5 m/min and STD = 1 mm; (**h**) P = 300 MPa, f = 0.5 m/min and STD = 1.5 mm; and (**i**) P = 300 MPa, f = 0.5 m/min and *STD = 1.5 mm*. (Substrate-deposit boundaries are marked with a dotted red line)

weld beads benefiting from low energy input levels with suitable values of AR and D were found to be those deposited using a speed of 800mm/min (i.e., beads in Fig. 6g-(i)). Therefore, laser power of 250W and scanning speed of 800mm/min were selected as the parameter set for performing the repair experiments using LMD.

3.2 Repair tests

3.2.1 Microstructure of the deposit

The images in Fig. 8 depict the substrate and deposit microstructures. Deposited material presents large columnar grains oriented along the build direction (BD) with epitaxial growth usually achieved in LMD process. The solidification is directly influenced by the orientation of the main heat flux, commonly perpendicular to substrate or pre-deposited layers. In Fig. 8 we are unable to highlight the presence of HAZ because it is very fine. In addition, the heat treatments induced by the deposition of upper layers tend to minimize it. However, the presence of a HAZ was revealed by the measurements of microhardness, as seen in Fig. 16. Figure 8 shows differently machined substrates, but with similar results observed in both. From these micrographs, the dilution was measured in the *x*-direction (perpendicular to the deposition strategy path) for all specimens as $\sim 130 \pm 20\ \mu m$, corresponding to that of single weld beads built at *250 W* and *800 mm/min*.

The images in Fig. 9 show the microstructure of laser deposited material as observed with an SEM fitted with an SE detector. Dendritic morphologies, namely cellular dendrites, were observed in all specimens as depicted in Fig. 9a-c. The cell morphology of dendrites is distinguished according to the orientation of the dendrite in the cutting-plane (Fig. 9b). Cellular dendrites are $\sim 5\ \mu m$ in size. Dendritic microstructure is a function of the thermal gradient and the solidification rate produced by LMD (Fig. 9d). When comparing the observed dendrites with the graph depicted in Fig. 9d, they correspond to the rather

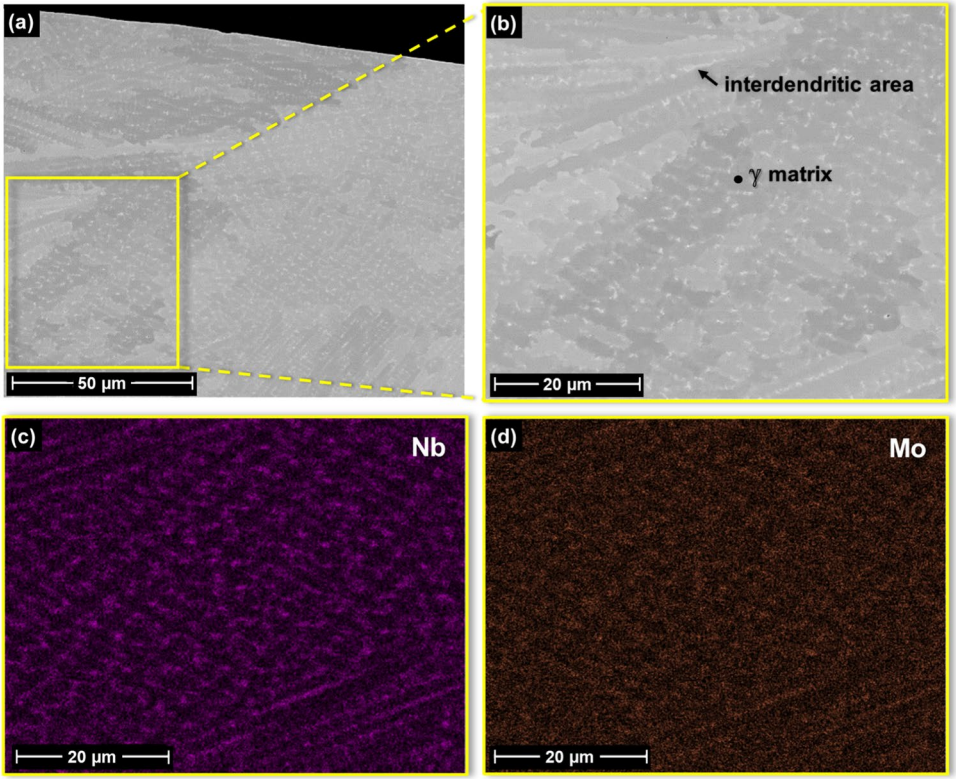

Fig. 11 SEM images taken from the IN718 deposit showing the inter-dendrite region at (**a**) × 1000 magnification and (**b**) × 2000 magnification and, elemental distributions of (**c**) Nb and (**d**) Mo in the deposit

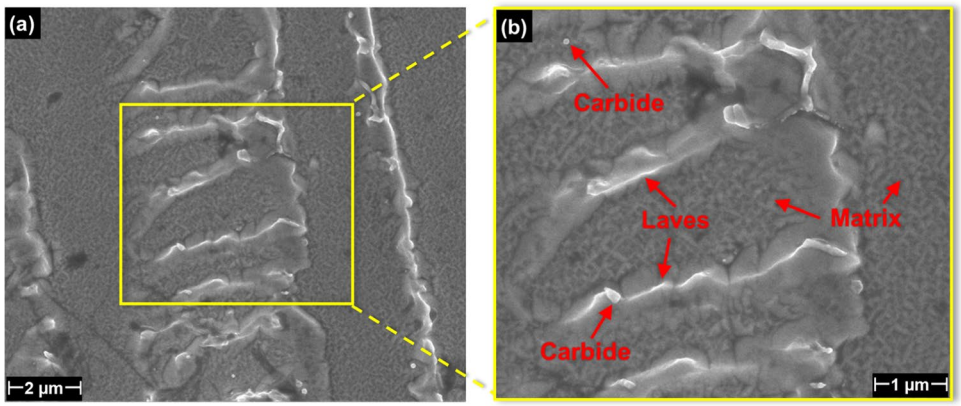

Fig. 12 SEM images (SE mode) with in-lens detector showing the main precipitates in IN718 deposited material. With: (**a**) at × 10,000 magnification and (**b**) at at × 20,000 magnification

thin cell type, indicating relatively high cooling rates due to the fineness of the cells.

Figure 10 shows the interface zone between the substrate and the deposited material for all the specimens. In Fig. 10a the substrate-deposit boundary is marked with a red dotted line. The micrographs showed a good metallurgical bond free of cracks for all different substrate conditions. These images also demonstrate that there is no influence of the different surface roughness and textures of the substrate on the quality of repair. This could be due, on the one hand, to LMD being performed using the same parameter set for all specimens, and on the other hand, to high dilution levels resulting from the laser deposition process (the higher roughness levels induced by AWJ machining corresponded to 25 µm).

Figure 11 reveals the dendritic structure of the printed material, with an interdendritic region shown in light contrast with respect to the darker dendritic core. The interdendritic region is seen to consist of small irregular and globular white zones. This interdendritic region was verified by EDS to have a high content of niobium (Fig. 11d) followed by molybdenum constituents, which is consistent with previous studies [2].

Higher magnification of the dendrite structure depicted in Fig. 12 shows Laves phase identified in white irregular shapes, as compared to the γ matrix rich in Nb, Mo

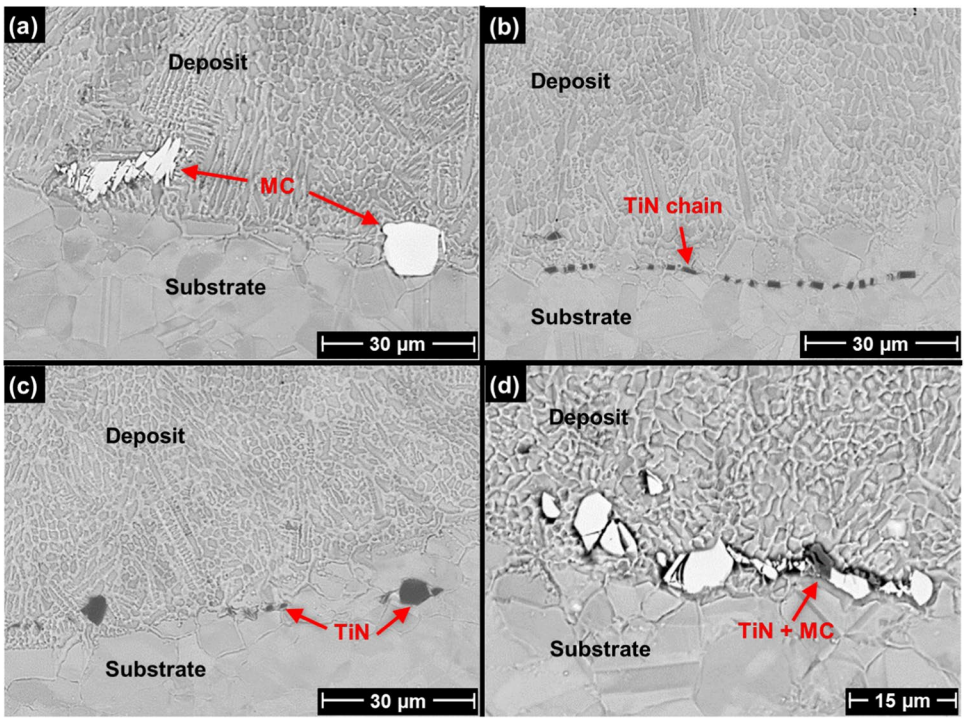

Fig. 13 SEM micrographs showing different type of precipitates at the substrate-deposit boundary in surfaces machined at (**a**) P = 200 MPa, f = 1 m/min and STD = 1 mm; (**b**) P = 250 MPa, f = 1 m/min and STD = 0.5 mm; (**c**) P = 300 MPa, f = 0.5 m/min and STD = 1 mm; and (**d**) P = 200 MPa, f = 1.5 m/min and STD = 1 mm

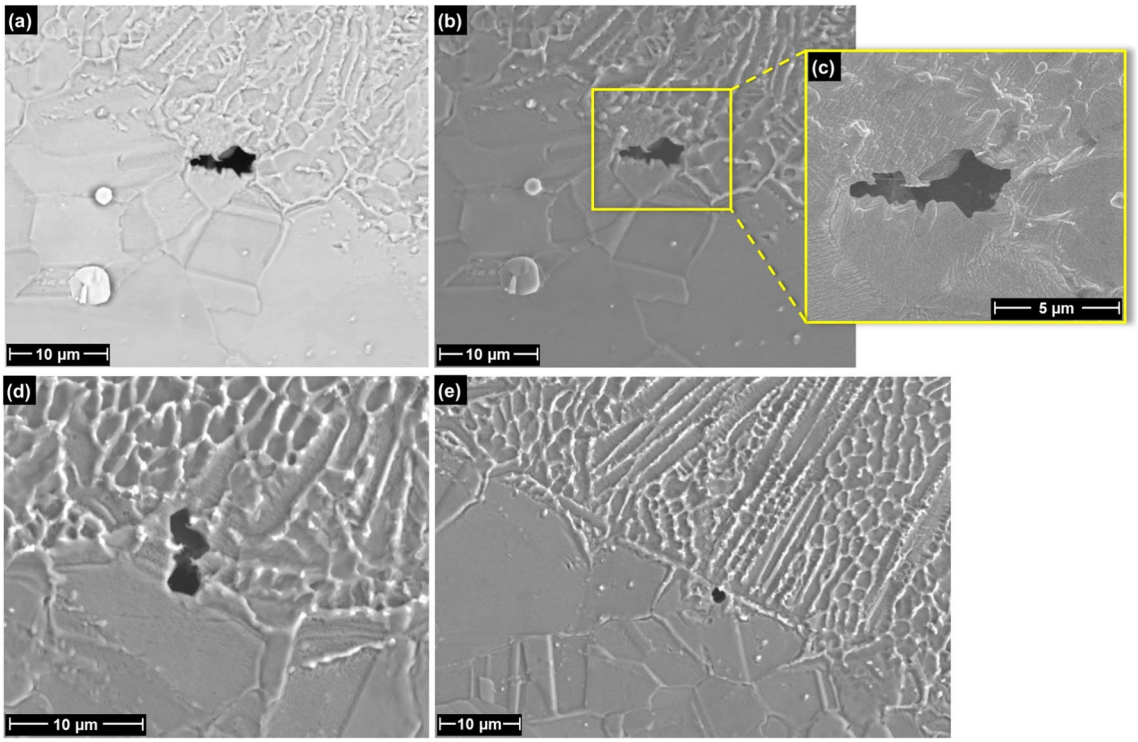

Fig. 14 SEM images showing void inclusions at the substrate-deposit boundary of substrate milled at P = 250 MPa, f = 0.5 m/min and STD = 1.5 mm with (**a**) BSE detector, (**b**) SE detector at × 3000 magnification and (**c**) at × 10,000 magnification with In-lens detector; BSE images of void inclusions in the interface of the substrates milled at (**d**) P = 250 MPa, f = 1 m/min and STD = 0.5 mm, and (**e**) P = 250 MPa, f = 0.5 m/min and STD = 1 mm

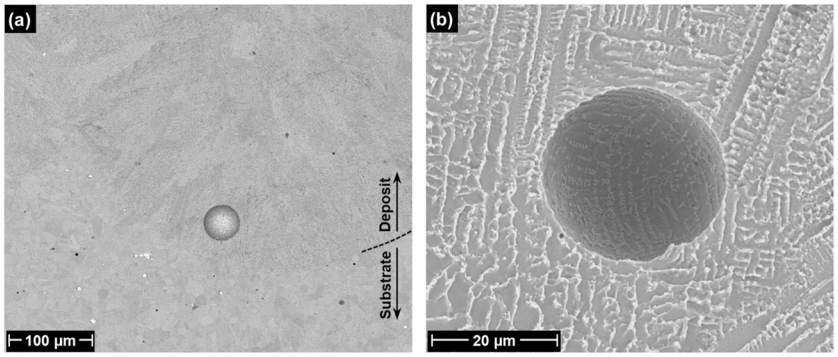

Fig. 15 SEM micrographs showing porosity in deposited layers in (**a**) BSE detector at 260 × magnification showing a large pore of ~ 40 µm in diameter and (**b**) SE detector at 2000 × magnification showing a pore exceeding 20 µm in diameter

and Ti, the principal elements of the Laves [3]. The size of Laves varied significantly from ~ 1–10 µm. Other than Laves, spherical or globular shaped very small precipitates are also observed in Fig. 12 and these could be identified as carbides, which are rich in Ti and Nb [3]. The presence of precipitates at or near the substrate-deposit interface was observed (Figs. 10 and 13). These random precipitate are found in different sizes ranging from a few microns to tens of microns. EDS analysis of these precipitates confirms two types of precipitates: dark polygonal or amorphous particles are titanium nitrides (TiN), and light globular amorphous particles correspond to MC type niobium carbides. EDS patterns of these precipitates are similar to those depicted in Fig. 10 for wrought IN718 substrate. It was observed that the precipitates can be distributed forming long chains of particles of several tens of microns in length as depicted in Fig. 13b, d. The precipitates can also be conglomerated with other as showed in Fig. 13d. A previous study [35] also reported the presence of these precipitates at the substrate-deposit interface.

Further examination of substrate-deposit interfaces shows few void inclusions of less than 10 µm as depicted in Fig. 14. They are randomly present at the substrate-deposit boundary in only 3 of the 9 specimens (i.e. substrates machined at P = 250 MPa, f = 0.5 m/min and STD = 1 mm; P = 250 MPa, f = 0.5 m/min and STD = 1.5 mm; and P = 250 MPa, f = 1 m/min and STD = 0.5 mm); this indicates that there is no specific trend relating deposition conditions to repair defects. Such defects have been also reported in [5, 15] and attributed to higher cooling rates along the non-preheated substrate, creating an instability of the melt pool, or as a result of restrictions of access of the laser beam along the outline of the substrate.

Scattered porosity was detected throughout the deposited layers in all specimens, as depicted in Fig. 15. The majority had a diameter of less than *5 µm,* though bigger pores of more than 20 µm were seen to be randomly located in the layers of some deposits. No correlation was found between the substrate milling conditions and porosity. The smaller porosities can be attributed to the pores originally present in the powder feedstock, and greater porosities to turbulences in the melt pool that occur during the deposition process [3].

Finally, in terms of residual grit on the substrate surface, EDS mapping analysis showed that there were no detectable traces of the grit. Neither was found at the substrate-deposit interface as expected, nor in the deposited layers. This could be due to the complex thermal movements taking place during the deposition process and the different fusion temperatures of the chemical components of the abrasive grit. Thus, it could be stated that residual grit in the substrate surface had no effect on the repair quality at the interface.

3.2.2 Microhardness

Vickers hardness profiles for the seven different substrate conditions are depicted in Fig. 16. For all specimens, the hardness values were seen to be higher in the deposited material than in the substrate, by ~ *50 HV*. The microhardness in the deposited layers ranges between *255* and *300 HV*. The higher hardness in the deposited material as compared to the substrate is mainly due to the annealing heat treatment that the substrate material was subjected to before being supplied, that is the as-received material plate. Annealing increases the ductility of the material and reduces its hardness. In contrast to existing literature, in [20] the authors report higher hardness in the substrate than in the deposited IN718, however the substrate has undergone a solution treatment before the LMD process. Also, in [26] it was stated that higher hardness in the substrate as compared to the deposit is due to the presence of twins in the substrate because twinning reduces the grain size. This is equivalent to a hardening mechanism, blocks dislocation movement and limits the movement of grain boundaries.

It was also observed from the microhardness profiles (Fig. 16) that the top of the deposit (*i.e.* last deposited layer) presented slightly lower hardness than the first deposited layers. This could be due to a thermal energy pile-up as the laser is used to build successive layers,

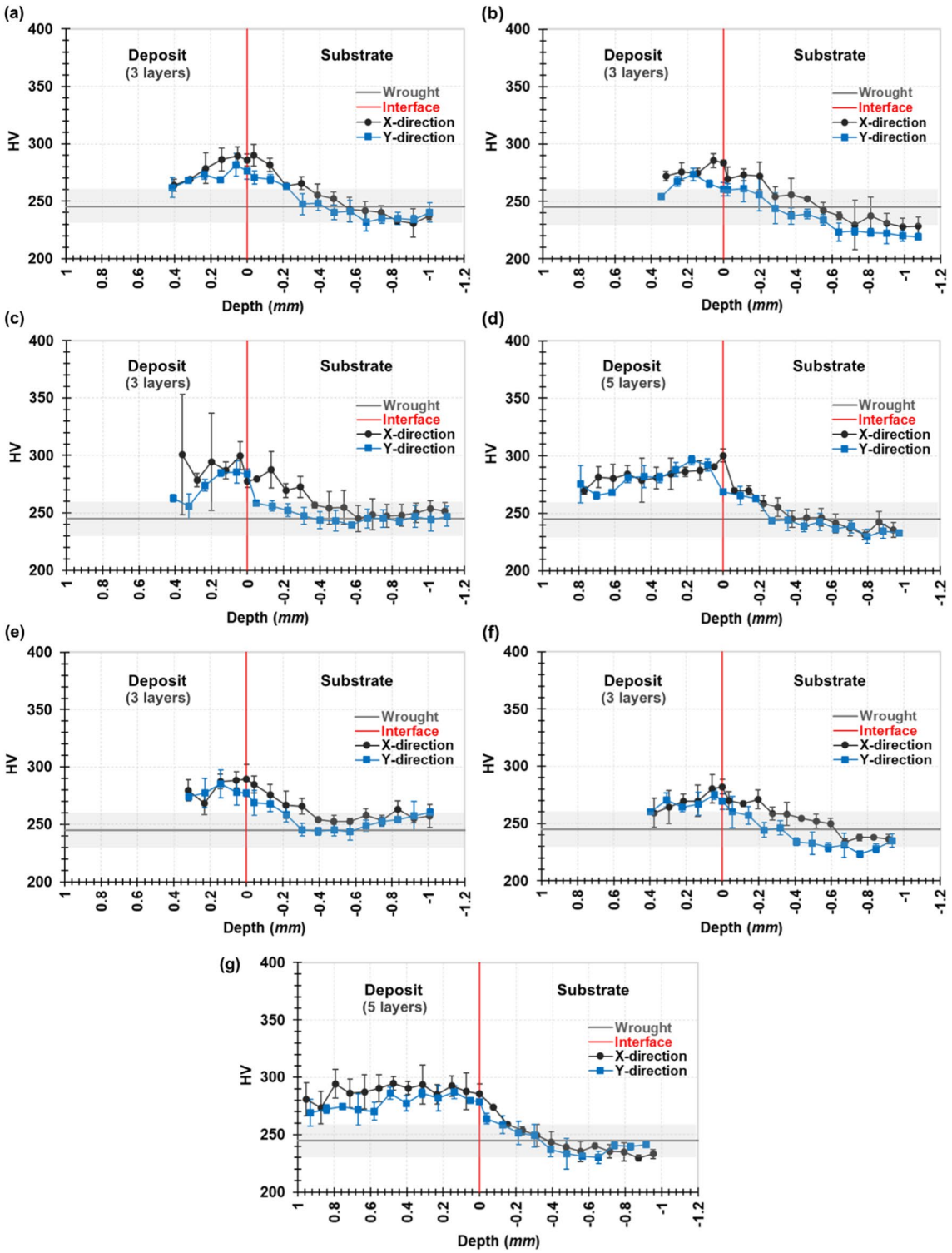

Fig. 16 Microhardness evolution from deposited material to the substrate milled at (**a**) P = 200 MPa, f = 1 mm/min and STD = 1 mm; **b** P = 200 MPa, f = 1.5 mm/min and STD = 1 mm; **c** P = 250 MPa, f = 0.5 mm/min and STD = 1 mm; **d** P = 250 MPa, f = 0.5 mm/min and STD = 1.5 mm; **e** P = 300 MPa, f = 0.5 mm/min and STD = 1 mm; **f** P = 300 MPa, f = 0.5 mm/min and STD = 1.5 mm; and (**g**) P = 250 MPa, f = 1 mm/min and STD = 0.5 mm. (x-direction is perpendicular to deposition path and y-direction is parallel to deposition path)

where the initial layers retain more thermal energy than the higher ones.

Finally, hardness values of ~ 280 HV were measured at the interface, with similar values in the adjacent substrate area, in all the specimens. Hardness values corresponding to that of wrought material were determined at depths of ~ 400 µm beneath the interface, indicating the areal extent of the HAZ created during LMD.

4 Conclusions

A parametric study was carried out to determine an optimal set of parameters for simulating repair of damaged parts made of IN718 alloy. The set of beads deposited was analysed for geometrical quality and extent of dilution, and laser power of 250W and scanning speed of 800 mm/min found to be the optimal process parameters. Repair was simulated by using LMD to refill grooves in wrought IN718 substrates, with different surface roughness values and textures induced by AWJ milling. Repair quality was determined according to the resulting microstructure, levels of porosity, and microhardness measurements, with particular emphasis on the substrate-deposit interface.

Based on this experimental investigation, the following conclusions can be drawn:

- A good metallurgical bond, free of cracks, was seen at the substrate-deposit interface for all simulated repairs. The HAZ could not be observed in micrographs due to the limited magnification, but its presence was clearly highlighted in the microhardness measurements. Randomly located void inclusions were seen at the substrate-deposit interfaces, as well as scattered porosity in the deposited material. Residual grit in the machined substrates was found to have no effect on the repair quality: it could be detected neither through general visual inspection nor through the use of SEM.
- In contrast to the homogeneous microstructure and small equiaxed grains of the Inconel 718 substrate, the microstructure of LMD-deposited material consisted of large columnar dendrites oriented along the build direction. Since the microstructure and microhardness values of the deposited material are very different from those of the substrate, post-deposition thermal treatments will be required to homogenise the microstructure across the substrate-deposit interface.
- The process parameters for both surface preparation and LMD deposition may be chosen independently of each other, but they need to be contained in specific recommended ranges. The deposition parameters are preponderant because they erase the effect of the AWJ machining.
- No effect of the substrate surface roughness and texture on repair quality was observed, mainly because the dilution is at least ~ 5 times greater than the highest surface roughness value ($Sa \approx 25\ \mu m$).
- In all of the experiments, deposited material showed a microhardness of ~ *100 HV* higher than that of the annealed wrought substrate. The hardness values in the deposited material ranged between *255* and *300 HV*, and the average hardness value at the interface was ~ *280 HV*.

Funding Open access funding provided by Université Toulouse III - Paul Sabatier.

Declarations

Conflict of interest As the corresponding author of the submitted paper, I declare the following on behalf of my co-authors:
• All authors have participated in (a) conception and design, or analysis and interpretation of the data; (b) drafting the article or revising it critically for important intellectual content; and (c) approval of the final version.
• This manuscript has not been submitted to, nor is under review at, another journal or other publishing venue.
• The authors have no affiliation with any organization with a direct or indirect financial interest in the subject matter discussed in the manuscript.
• The authors of this paper certify that they have NO affiliations with or involvement in any organization or entity with any financial interest (such as honoraria; educational grants; participation in speakers' bureaus; membership, employment, consultancies, stock ownership, or other equity interest; and expert testimony or patent-licensing arrangements), or non-financial interest (such as personal or professional relationships, affiliations, knowledge or beliefs) in the subject matter or materials discussed in this manuscript.

References

1. Colorado HA, Gutierrez Velasquez EI, Neves Monteiro S (2020) Sustainability of additive manufacturing: the circular economy of materials and environmental perspectives. J Mater Res Technol 9:8221–8234. https://doi.org/10.1016/j.jmrt.2020.04.062
2. Ding RG, Huang ZW, Li HY, Mitchell I, Baxter G, Bowen P (2015) Electron microscopy study of direct laser deposited IN718. Mater Charact 106:324–337. https://doi.org/10.1016/j.matchar.2015.06.017

3. Parimi LL, Aasa RG, Clark D, Attallah MM (2014) Microstructural and texture development in direct laser fabricated IN718. Mater Charact 89:102–111. https://doi.org/10.1016/j.matchar.2013.12.012
4. Wilson JM, Piya C, Shin YC, Zhao F, Ramani K (2014) Remanufacturing of turbine blades by laser direct deposition with its energy and environmental impact analysis. J Clean Prod 80:170–178. https://doi.org/10.1016/j.jclepro.2014.05.084
5. Onuike B, Bandyopadhyay A (2019) Additive manufacturing in repair: Influence of processing parameters on properties of Inconel 718. Mater Lett 252:256–259. https://doi.org/10.1016/j.matlet.2019.05.114
6. Imam HZ, Al-Musaibeli H, Zheng Y, Martinez P (2023) R Ahmad (2023) Vision-based spatial damage localization method for autonomous robotic laser cladding repair processes. Robot Comput-Integr Manuf 80:102452. https://doi.org/10.1016/j.rcim.2022.102452
7. Avram O, Fellows C, Menerini M, Valente A (2021) Automated platform for consistent part realization with regenerative hybrid additive manufacturing workflow. Int J Adv Manuf Technol 119:1737–1755. https://doi.org/10.1007/s00170-021-08218-5
8. Li L, Li C, Tang Y, Yanbin Du (2017) An integrated approach of reverse engineering aided remanufacturing process for worn components. Robot Comput-Integr Manuf 48:39–50. https://doi.org/10.1016/j.rcim.2017.02.004
9. Al-Musaibeli H, Ahmad R (2022) A path planning method for surface damage repair using a robot-assisted laser cladding process. Int J Adv Manuf Technol 122:1259–1279. https://doi.org/10.1007/s00170-022-09933-3
10. Zhong C, Gasser A, Kittel J, Wissenbach K, Poprawe R (2016) Improvement of material performance of Inconel 718 formed by high deposition-rate laser metal deposition. Mater Des 98:128–134. https://doi.org/10.1016/j.matdes.2016.03.006
11. Selcuk C (2011) Laser metal deposition for powder metallurgy parts. Powder Metall 54(2):94–99. https://doi.org/10.1179/174329011X12977874589924
12. Knüttel D, Baraldo S, Valente A, Wegener K, Carpanzano E (2022) Transfer learning of neural network based process models in direct metal deposition. Procedia CIRP 107:863–868. https://doi.org/10.1016/j.procir.2022.05.076
13. Stevens EL, Toman J, To AC, Chmielus M (2017) Variation of hardness, microstructure, and Laves phase distribution in direct laser deposited alloy 718 cuboids. Mater Des 119:188–198. https://doi.org/10.1016/j.matdes.2017.01.031
14. Sui S, Chen J, Ming X, Zhang S, Lin X, Huang W (2017) The failure mechanism of 50% laser additive manufactured Inconel 718 and the deformation behavior of Laves phases during a tensile process. Int J Adv Manuf Technol 91(5):2733–2740. https://doi.org/10.1007/s00170-016-9901-9
15. Johnson AS, Shao S, Shamsaei N, Thompson SM, Bian L (2017) Microstructure, fatigue behavior, and failure mechanisms of direct laser-deposited inconel 718. JOM 69(3):597–603. https://doi.org/10.1007/s11837-016-2225-2
16. Zhong C, Gasser A, Kittel J, Fu J, Ding Y, Poprawe R (2016) Microstructures and tensile properties of Inconel 718 formed by high deposition-rate laser metal deposition. J Laser Appl 28(2):022010. https://doi.org/10.2351/1.4943290
17. Tian Y et al (2014) Rationalization of microstructure heterogeneity in INCONEL 718 builds made by the direct laser additive manufacturing process. Metall Mater Trans A 45(10):4470–4483. https://doi.org/10.1007/s11661-014-2370-6
18. Dinda GP, Dasgupta AK, Mazumder J (2012) Texture control during laser deposition of nickel-based superalloy. Scripta Mater 67(5):503–506. https://doi.org/10.1016/j.scriptamat.2012.06.014
19. Kumar LJ, Nair CGK (2017) Laser metal deposition repair applications for Inconel 718 alloy. Mater Today: Proceedings 4(10):11068–11077. https://doi.org/10.1016/j.matpr.2017.08.068
20. Tabernero I, Lamikiz A, Martínez S, Ukar E, Figueras J (2011) Evaluation of the mechanical properties of Inconel 718 components built by laser cladding. Int J Mach Tools Manuf 51(6):465–470. https://doi.org/10.1016/j.ijmachtools.2011.02.003
21. Sreekanth S, Ghassemali E, Hurtig K, Joshi S, Andersson J (2020) Effect of direct energy deposition process parameters on single-track deposits of alloy 718. Metals 10(1):1. https://doi.org/10.3390/met10010096
22. Piscopoa G, Atzeni E, Biamino S, Iuliano L, Mazzucato F, Saboori A, Salmi A, Valente A (2022) Analysis of single tracks of IN718 produced by laser powder directed energy deposition process. Procedia CIRP 112:340–345. https://doi.org/10.1016/j.procir.2022.09.006
23. Mazzucato F, Forni D, Valente A, Cadoni E (2021) Laser metal deposition of inconel 718 alloy and as-built mechanical properties compared to casting. Materials. https://doi.org/10.3390/ma14020437
24. Wei HL, Mukherjee T, DebRoy T (2016) Grain growth modeling for additive manufacturing of nickel based superalloys. Proceedings of the 6th International Conference on Recrystallization and Grain Growth (ReX&GG), pp 265–269
25. Sui S, Chen J, Zhang R, Ming X, Liu F, Lin X (2017) The tensile deformation behavior of laser repaired Inconel 718 with a non-uniform microstructure. Mater Sci Eng, A 688:480–487. https://doi.org/10.1016/j.msea.2017.01.110
26 Lambarri J, Leunda J, GarcíaNavas V, Soriano C, Sanz C (2013) Microstructural and tensile characterization of Inconel 718 laser coatings for aeronautic components. Opt Lasers Eng 51(7):813–821. https://doi.org/10.1016/j.optlaseng.2013.01.011
27. Izadi M, Farzaneh A, Mohammed M, Gibson I, Rolfe B (2020) A review of laser engineered net shaping (LENS) build and process parameters of metallic parts. Rapid Prototyp J 26(6):1059–1078. https://doi.org/10.1108/RPJ-04-2018-0088
28. Liu Z, Kim H, Liu W, Cong W, Jiang Q, Zhang H (2019) Influence of energy density on macro/micro structures and mechanical properties of as-deposited Inconel 718 parts fabricated by laser engineered net shaping. J Manuf Process 42:96–105. https://doi.org/10.1016/j.jmapro.2019.04.020
29. Liu D, Lippold JC, Li J, Rohklin SR, Vollbrecht J, Grylls R (2014) Laser engineered net shape (LENS) technology for the repair of ni-base superalloy turbine components. Metall and Mat Trans A 45(10):4454–4469. https://doi.org/10.1007/s11661-014-2397-8
30. Cano-Salinas L et al (2023) Effect of process parameters of Plain Water Jet on the cleaning quality, surface and material integrity of Inconel 718 milled by Abrasive Water Jet. Tribol Int 178:108094. https://doi.org/10.1016/j.triboint.2022.108094
31. Vander Voort G, Manilova E (2004) Metallographic techniques for superalloys. Microsc Microanal 10, août. https://doi.org/10.1017/S1431927604883442
32. Dalaee M, Cerrutti E, Dey I, Leinenbach C, Wegener K (2022) Parameters development for optimum deposition rate in laser dmd of stainless steel EN X3CrNiMo13-4. Lasers Manuf Mater Process 9(1):1–17. https://doi.org/10.1007/s40516-021-00161-3

33. Dass A, Moridi A (2019) State of the art in directed energy deposition: from additive manufacturing to materials design. Coatings 9(7):7. https://doi.org/10.3390/coatings9070418
34. Kou S (2003) Welding metallurgy, 2nd edn. Wiley Interscience, New Jersey. https://doi.org/10.1002/0471434027
35. Lei Z, Lu N, Yu X (2019) Epitaxy and new stray grain formation mechanism during epitaxial laser melting deposition of Inconel 718 on directionally solidified nickel-based superalloys. J Manuf Process 42:11–19. https://doi.org/10.1016/j.jmapro.2019.04.016